Research Article Vol. 58, No. 2 / 10 January 2019 / Applied Optics 389

applied optics

Multi-step phase aberration compensation method based on optimal principal component analysis and subsampling for digital holographic microscopy

Xiangyu Zhang,[1,2,3,†] Jiasong Sun,[1,2,3,†] Zuxin Zhang,[1,2,3] Yao Fan,[1,2,3] Qian Chen,[1,2] and Chao Zuo[1,2,3,4,*]

[1]School of Electronic and Optical Engineering, Nanjing University of Science and Technology, No. 200 Xiaolingwei Street, Nanjing, Jiangsu Province 210094, China
[2]Jiangsu Key Laboratory of Spectral Imaging & Intelligent Sense, Nanjing, Jiangsu Province 210094, China
[3]Smart Computational Imaging Laboratory (SCILab), Nanjing University of Science and Technology, Nanjing, Jiangsu Province 210094, China
[4]e-mail: zuochao@njust.edu.cn
*Corresponding author: surpasszuo@163.com

Received 6 September 2018; revised 26 November 2018; accepted 4 December 2018; posted 4 December 2018 (Doc. ID 345169); published 7 January 2019

Digital holographic microscopy (DHM) is a well-known powerful technique allowing measurement of the spatial distributions of both the amplitude and phase produced by a transparent sample. Nevertheless, in order to improve the transverse resolution of the DHM system, a microscope objective has to be introduced in the object beam path, which inevitably leads to phase aberration in the object wavefront. In recent decades, a multitude of techniques have been proposed to compensate for this phase aberration, and the principal component analysis (PCA) technique has proven to be one of the most promising approaches due to its high compensation accuracy, low computational complexity, and simplicity to implement. However, when it comes to high-order phase aberration, which is common for a mal-aligned DHM system, the PCA technique usually performs poorly since it is unable to fit the cross-terms of the standard Zernike polynomials. To address this problem, here we propose a multi-step phase-aberration-compensation method based on optimal PCA and sub-sampling where PCA is first applied to remove the non-cross-aberration terms, followed by sub-sampled fitting for the remaining cross-aberration correction. The key advantage of our approach is that it can handle both the conventional objective phase curvature and high-order aberrations such as astigmatism and anamorphism with very little computational overhead. Simulation and experimental results demonstrate that our method outperforms state-of-the-art approaches, and the compensation results are consistent with those obtained from the double-exposure method. © 2019 Optical Society of America

https://doi.org/10.1364/AO.58.000389

1. INTRODUCTION

Digital holography is a well-known, powerful technique allowing quantitative amplitude and phase-contrast microscopy, as well as detection of changes in optical path length with sub-wavelength interferometric sensitivity. The numerically reconstructed holographic image contains both amplitude and phase information of the object wave. In combination with microscopic resolution, this offers new possibilities for detecting refractive index changes and variations in the morphology of transparent cellular samples [1–6]. For the interdisciplinary fields of biomedicine [7–10], life sciences [11–14], bio-engineering [15,16], and biophotonics [17–19], digital holographic microscopy (DHM) has opened up new perspectives for the visualization and quantification of the integral cellular refractive index, cell drymass, and, for adherent grown cells, cell shape in a nondestructive, real-time (more than 25 frames per second, 1024 × 1024 pixel), marker-free (unlabeled), and full-field (no scanning required) manner. Nevertheless, in order to improve the transverse resolution of the DHM system, a microscope objective has to be introduced in the object beam path, which inevitably causes a spherical wavefront in the object wave field that generates phase curvature in the reconstructed wave field. This phase aberration should be compensated in order to accurately determine the phase delay induced by the measured specimen [20–23].

In past decades, a multitude of techniques have been proposed with the aim to remove such phase aberrations, which can be categorized into two categories: physical [24–28] and numerical [21,23,29–36]. Physical compensation methods are generally achieved through introducing the same wavefront curvature in the reference beam by introducing either a same-objective lens [24–26] or position-adjustable lens [26], or by adopting a bi-telecentric optical configuration [27,28], which can only provide partial aberration. In practice, these methods are difficult to implement due to the complicated optical system configuration and the requirement for a precise alignment of all the optical elements involved. The numerical compensation methods, in contrast, compensate the phase aberration through post-processing of the digital hologram or the reconstructed phase. The most straightforward method of this category is double exposure [31,32], in which a reference hologram needs to be recorded without the presence of specimen. Subtraction of the reference phase from the original phase map produces a quantitative phase map completely free of aberrations. However, in most practical applications, the phase aberration may drift with the changes of focus and other experimental conditions, necessitating repeated and elaborated re-calibration. As a result, reference-free methods have been studied to continuously compensate the phase aberration without using references and interrupting observation. In most reference-free methods, a phase mask (i.e., the estimate of aberration) is created and applied to either the reconstruction or hologram plane. In order to get the phase mask, Colomb *et al.* [33] proposed a general fitting procedure applied on specimen areas known to be flat. However, the pre-knowledge about the setup or/and specimen under test is difficult to obtain beforehand. Therefore, in most cases, the phase mask can only be estimated by directly applying Zernike polynomial fitting [29] or two-dimensional (2D) least-square fitting [23] on the whole phase map. As a result, these approaches face a relatively heavy computational burden. Moreover, the estimate of phase mask is prone to be deviated by the phase values of areas occupied by the sample. This problem was explicitly considered in the recent deep-learning-based phase-error-compensation approach [30], in which the sample-free region is detected based on a convolutional neural network that allows for Zernike polynomial fitting to obtain a much more reliable phase mask which is undisturbed by the sample phase. However, the success of the deep-learning-based approach is largely dependent on abundant ground truth training datasets, which are often unavailable or at least require massive human intervention.

Principal component analysis (PCA), a well-known statistical tool that uses an orthogonal transformation to convert a large set of variables to a small set of linearly uncorrelated variables (called principal components) that still contain most of the information in the large set, has been widely used in statistics, machine learning, and information theory, where data analysis is preferably done in a dimension-reduced space rather than the original space for higher accuracy and lower complexity [21]. Due to its effectiveness in dimensionality reduction and feature extraction, a PCA algorithm has been introduced in DHM as an efficient tool to extract the phase-aberration term from the first principal component of the phase distribution [21]. The advantages of the PCA method are threefold. First, with the help of the implicit eigen-filtering nature of PCA, the phase-aberration term can be automatically separated from the sample phase with much less perturbation. Second, by separating the aberration terms to two singular vectors, phase unwrapping and fitting of the data is reduced to one dimension, which significantly improves compensating efficiency and phase-unwrapping accuracy. Finally, by implementing PCA only on the reduced-sized spectrum where the aberration term is concentrated on, the compensation accuracy can be further improved, and meanwhile the computation time can be further reduced [36]. Despite all these advantages, the validity of the PCA approach relies on the pre-condition that the phase-aberration function can be broken down into two dominant vectors along the x and y axes, leaving cross and higher-order terms of the standard polynomial unaccounted for. However, such aberrations are not uncommon for DHM systems in which the beam paths are misaligned, or low-quality optical elements are employed.

To this end, here we propose a multi-step phase-aberration-compensation method based on optimal PCA and sub-sampling (MOPCA), where PCA is first applied to remove the non-cross-aberration terms and then the 2D polynomial fitting is performed on the sub-sampled residual phase map to extract the cross-aberration term. The key advantage of our approach is that it can handle both the conventional objective phase curvature as well as the cross- and higher-order aberrations, such as astigmatism and coma, with very little computational overhead. As a result, MOPCA preserves all the advantages of the PCA approach while effectively compensating for its deficiencies. Thus, the universality and versatility of the PCA-based phase-aberration-compensation algorithm are significantly enhanced. Simulation and experimental results demonstrate that our method outperforms state-of-the-art approaches, and the compensation results are consistent with those obtained from the double-exposure method, even in the presence of significant cross- and higher-order aberrations.

2. PRINCIPLE

A. Phase Aberration Model in DHM

Digital holography consists of recording a digitized hologram using an electronic device [e.g., a charge coupled device (CCD)], and later reconstructing the hologram numerically with a computer. A digital hologram is created by interference; that is, an unknown wavefront coming from the object, called object wave, is combined with the reference wave to produce a fringe pattern modulated by the phases of the two waves. For the off-axis configuration (there exists a small angle between the object wave and reference wave), the intensity distribution of the hologram can be presented as

$$I_H = |O|^2 + |R|^2 + RO^* + R^*O, \tag{1}$$

where $R(x, y)$ and $O(x, y)$ are the reference and object waves, and * denotes the complex conjugate. Due to the small angle between the reference and object waves, the virtual image term can be extracted by filtering the hologram's 2D spectrum:

$$I_H^F = |R||O| \exp[j\varphi(x,y)]Q(x,y), \quad (2)$$

where $I_H^F(x,y)$ is the Fourier spectrum of the virtual image, j is the imaginary unit, $\varphi(x,y)$ is the phase of the test object, and $Q(x,y)$ is the phase-aberration term needed to be compensated.

In the traditional phase-aberration model in DHM, the phase aberration mainly consists of two parts: the spherical term induced by the microscope objective and the tilt term caused by the off-axis geometry. Thus, $Q(x,y)$ can be represented as

$$Q(x,y) = \exp[j(k_x x + k y_y)] \exp[j(l_x x^2 + l_y y^2)], \quad (3)$$

where factors k_x and k_y denote the linear phase difference between O and R due to the off-axis geometry. The parameters l_x and l_y describe the phase divergence caused by the mismatch in spherical phase curvature.

When the aberration term $Q(x,y)$ is obtained, its conjugate $Q^*(x,y)$ can be multiplied with the filtered hologram, leading to an aberration-free virtual image:

$$Q^*(x,y) I_H^F(x,y) = |R||O| \exp[j\varphi(x,y)]. \quad (4)$$

However, in addition to the spherical and tilt aberration terms, high-order non-cross and cross-aberration terms such as coma and astigmatism caused by the misalignment of the optical path, which are not uncommon, are also contained in DHM. Therefore, $Q(x,y)$ can be rewritten as

$$Q(x,y) = \exp\left[j \sum_{n=1,p=1,q=1}^{N} (a_n x^n + b_n y^n + c_{p,q} x^p y^q)\right], \quad (5)$$

where a_n, b_n are the coefficients of nth-order non-cross aberration x^n, y^n, respectively, and $c_{p,q}$ is the coefficient of cross-aberration term $x^p y^q$.

B. High-Order Phase Aberration Compensation Based on PCA

The phase-aberration-compensation method based on PCA can automatically extract the phase-aberration term into the first principal component, which is then broken down along the x and y axes to convert the 2D surface fitting and 2D phase unwrapping into 1D procedures in two orthogonal directions. For small objects with sparse distribution, the PCA-based method can provide fast and accurate phase-aberration compensation, of which the block diagram is shown in Fig. 1.

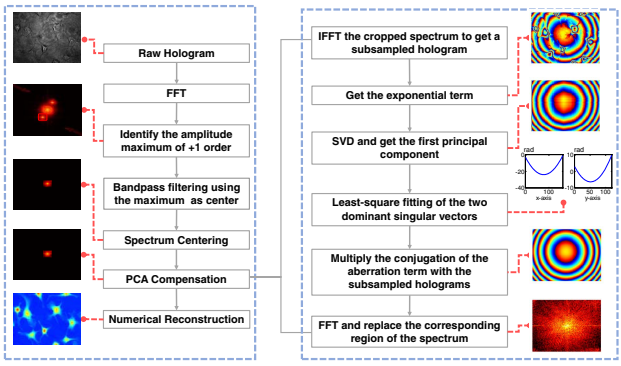

Fig. 1. Block diagram of PCA-based phase-aberration compensation method.

Observing Eq. (5), it can be found that the ideal model for aberration $Q(x,y)$ is a rank one matrix when only non-cross-aberration terms exist, which means that the phase-aberration matrix should only have one principal component. To illustrate this point, we simulate an aberration term with a unit amplitude and a phase containing second- and third-order non-cross-aberration terms, of which the resolution is 1280×960 and the pixel size is 0.5 μm; these parameters are used in the all simulations in this paper:

$$Q(x,y) = \exp\{j[(a_3 x^3 + b_3 y^3) + (a_2 x^2 + b_2 y^2)]\}, \quad (6)$$

where $a_3 = b_3 = 8$ and $a_2 = b_2 = 4$.

Figure 2(a) shows the wrapped phase of the non-cross-aberration term $Q(x,y)$. After PCA, the phase reconstructions using the first, first two, and first three principal components are shown in Figs. 2(b)–2(d), respectively. It can be seen that the difference between the aberration phase reconstructed from the first, first two, and first three components can be ignored, and the aberration is extracted to the first principal component. Furthermore, the singular value of the first principal component is 10^{14} times more than that of the second principal component, which fully satisfies the requirement for approximation using the first principal component. In addition, the 2D phase-unwrapping process is transformed into two 1D phase-unwrapping processes after PCA. The wrapped phase of the two dominant vectors is shown in Figs. 2(e) and 2(f), of which the unwrapped phase is shown in Figs. 2(g) and 2(h).

From the results shown in Fig. 2, it can be seen that the PCA-based method can provide accurate and fast compensation for high-order phase aberration, and only the fitting order needs to be adjusted. In order to further accelerate the speed, an optimal PCA-based (OPCA) method is proposed in Ref. [36], where PCA is implemented on the reduced-sized spectrum where the aberration is concentrated on, and the compensation accuracy can be further improved since the unrelated spectrum information is rejected through spectrum filtering. When applying Fourier transform (FT), we are actually implementing discrete FT (DFT) on the discrete sequence, which has an assumption that the sequence is periodic; this will cause boundary errors. Therefore, the first and the last points of the sequence need to be removed when fitting the dominant vectors.

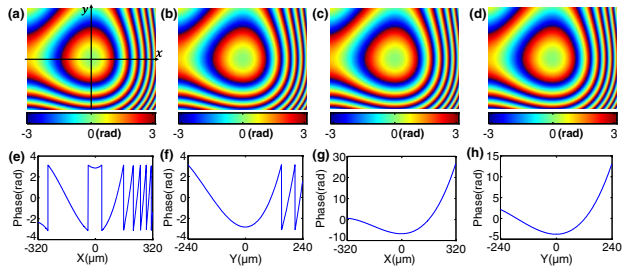

Fig. 2. Phase of non-cross-aberration terms and the results of PCA. (a) Original phase map. (b) Phase formed from the first principal component. (c) and (d) show the phase reconstructed from the first two and three principal components. (e) and (f) show the wrapped phase of the left and right dominant singular vectors of the first principal component. (g) and (h) show the unwrapped phase of the left and right dominant singular vectors of the first principal component.

To verify the effectiveness of the OPCA method for high-order non-cross-aberration terms, the following simulation is performed. We simulate three aberration terms with unit amplitude and phase containing the third-, fourth-, and fifth-order non-cross terms of x and y, respectively:

$$Q_1(x,y) = \exp[j(a_3x^3 + b_3y^3)], \tag{7}$$

$$Q_2(x,y) = \exp[j(a_4x^4 + b_4y^4)], \tag{8}$$

$$Q_3(x,y) = \exp[j(a_5x^5 + b_5y^5)], \tag{9}$$

where $a_3 = b_3 = 2$, $a_4 = b_4 = 1.6$, and $a_5 = b_5 = 3.2$.

The wrapped phase of each order aberration term is shown in Figs. 3(a)–3(c). After FT, the spectrum is obtained [Figs. 3(d)–3(f)]. In order to accelerate the operation speed of PCA, a small area in the middle of the spectrum is intercepted to obtain the sub-sampled spectrum [Figs. 3(g)–3(i)], of which the size is 40 × 30. After inverse FT (IFT), the phase map of the sub-sampled aberration is shown in Figs. 3(j)–3(l). In order to avoid the ringing effect caused by spectrum truncation, the phase map is up-sampled to get the full-resolution aberration phase map [Figs. 3(m)–3(o)].

In the simulation, the root mean square errors (RMSEs) between the recovered phase of the third-, fourth-, and fifth-order aberrations and their corresponding true phases are 0.0085 (rad), 0.0420 (rad), and 0.0491 (rad). Compared to the value of their corresponding true phase, the RMSEs can be ignored, and the phase recovered using this method meets the requirement of accuracy.

It is proved that the sub-sampling method in OPCA is suitable for the phase reconstruction of high-order non-cross-aberration terms through this simulation, and we find that the spectrum shape of each order aberration changes as the order increases. Therefore, the size of the intercepted area needs to be appropriately selected to contain as much energy as possible when intercepting the spectrum.

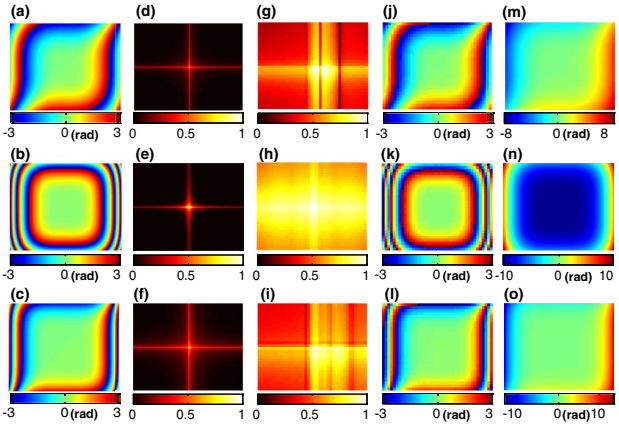

Fig. 3. Results of OPCA method for each order aberration. (a), (b), and (c) show the wrapped phase of $Q_1(x,y)$, $Q_2(x,y)$, and $Q_3(x,y)$. (d), (e), and (f) show the respective full-resolution normalized aberration spectra. (g), (h), and (i) show the respective sub-sampled normalized aberration spectra. (j), (k), and (l) show the sub-sampled phase recovered from each sub-sampled aberration spectrum. (m), (n), and (o) show the up-sampled phase of the aberration.

C. Phase Error Compensation in the Presence of Cross-Aberration Term

DHM not only contains non-cross-aberration terms, but also contains cross-aberration terms such as xy, which is known as vertical astigmatism often caused by the misalignment of the optical path; they can be expressed in the form of Eq. (5). PCA-based phase-aberration method can only provide appropriate compensation for non-cross-aberration terms, which is a rank 1 matrix, while the rank of the aberration matrix is not 1 in the existence of cross-aberration terms, which means that the aberration term cannot be extracted to one single component. Thus, the problem of phase-aberration compensation in the existence of cross-aberration terms is discussed.

First, the effectiveness of the OPCA method for cross-aberration terms, such as astigmatism, is investigated. An aberration of which the amplitude is unity and the phase only contains cross term xy is simulated:

$$Q(x,y) = \exp[j(c_{1,1}xy)], \tag{10}$$

where $c_{1,1} = 14$.

The phase of the cross-aberration term is shown in Fig. 4(a). After PCA, the phase reconstructions using the first, first two, and first three principal components are shown in Figs. 4(b)–4(d), respectively. It can be seen that the difference between the phases reconstructed using the first, first two, and first three principal components is large, and the reconstructed phase gradually approaches the original phase as the number of principal components used for phase reconstruction increases. Furthermore, the singular value of the first principal component and those of the second and third principal components are almost the same, and the aberration phase is not concentrated in one single component. Thus, PCA-based compensation method is incapable of removing the cross-aberration term xy, and the 2D fitting cannot be converted into two 1D fittings. So the nonlinear least-squares fitting method is adopted to fit the aberration directly. However, the time required for 2D fitting of the full-resolution phase map shown in Fig. 4(a) is about 22 s, which is too long to accept. Besides, the fitting speed is directly related to the size of the image for fitting. Therefore, inspired by the sub-sampling method in OPCA,

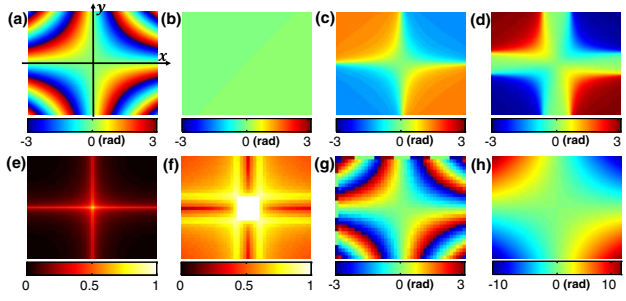

Fig. 4. PCA results of cross-aberration term xy and the sub-sampled 2D fitting. (a) Original phase map. (b) shows the phase reconstructed from the first principal component. (c) and (d) show the phase reconstructed from the first two and three principal components. (e) Full-resolution normalized aberration spectrum. (f) Normalized aberration spectrum after sub-sampling. (g) Phase recovered from the sub-sampled aberration spectrum. (h) Phase map recovered through up-sampling.

a simple way to accelerate the speed is to intercept a smaller spectrum. Considering that the energy of cross-aberration term xy mainly resides in the low-frequency domain [Fig. 4(e)], a 40×30 aberration spectrum of the cross term xy [Fig. 4(f)] is cropped, which is shown in Fig. 4(f). After IFT, the sub-sampled phase map is obtained [Fig. 4(g)]. A 2D phase-unwrapping method based on sorting by reliability following a non-continuous path is used to unwrap phase. At this point we can find that, due to the complexity of the 2D phase unwrapping, the speed and accuracy using a sub-sampled image are both high, compared to that using the full-resolution image. Similarly, since the 2D FT is actually implemented using the 2D DFT, which has a periodic assumption that the image is periodic, this will cause a boundary error. Thus, we need to remove the first and last rows and columns before aberration fitting. Furthermore, in order to avoid the ringing effect caused by spectrum truncation, the phase is up-sampled to get the full-resolution aberration phase map [Fig. 4(h)].

Through simulation, it can be found that the RMSE of the recovered phase is 0.0016 (rad), which can be ignored compared to the value of the true phase, which satisfies the required fitting accuracy. We also find that the RMSE increases as the size of the intercepted spectrum decreases, and a 40×30 spectrum contains more than 80% energy of the whole $+1$ spectrum; this meets the requirement for accurate phase recovery for most aberration terms, and the time spent using a 40×30 spectrum window is also acceptable.

D. Multi-Step Phase Aberration Compensation Based on OPCA and Sub-sampling

From the previous discussions in Sections 2.B and 2.C, it can be seen that although phase-aberration-compensation methods based on PCA or OPCA are efficient, they are only applicable to the compensation of non-cross-aberration terms, and not suitable for the compensation of cross-aberrations terms. Therefore, under circumstances in which high-order non-cross and cross-aberration terms coexist, the aberration cannot be compensated using only the OPCA method. Therefore, we propose a multi-step phase-aberration-compensation method based on OPCA and sub-sampling (MOPCA), which is suitable for situations in which the hologram contains non-cross and cross-aberration terms at the same time. For non-cross-aberration terms, the aberration can be compensated using the OPCA method, and then the residual cross-aberration terms can be fitted by performing 2D fitting on the sub-sampled residual phase map. The accurate full-resolution phase map can be obtained after up-sampling. A block diagram of the compensation process is shown in Fig. 5.

3. SIMULATION

Since the efficiency and accuracy of the previous methods are verified under the circumstance in which only individual aberration terms exist, we now discuss the effectiveness of the MOPCA method when high-order non-cross and cross-aberration terms coexist through simulation. First, an aberration in which the amplitude is unity and the phase contains second- and third-order non-cross terms and cross term xy is simulated:

$$Q(x,y) = \exp\{j[(a_2x^2 + b_2y^2) + (a_3x^3 + b_3y^3) + c_{1,1}xy]\}, \tag{11}$$

where $a_2 = b_2 = 6$, $a_3 = b_3 = 2.4$, and $c_{1,1} = 8$.

The wrapped phase is shown in Fig. 6(a), and an area of size 40×30 located in the center of the full-resolution spectrum is cropped [Fig. 6(b)]. After IFT, the recovered wrapped phase is shown in Fig. 6(c). The phase of the first principal component [Fig. 6(d)] and the residual phase [Fig. 6(e)] can be obtained after PCA. The two extracted 1D vectors are fitted along the x- and y-axes to obtain the correct sub-sampled phase map. For the residual phase aberration excluding the first principal component, considering the fact that its phase is not concentrated in one single component, a 2D fitting method based on least-square fitting is implemented to recover the correct sub-sampled phase map [Fig. 6(g)]. Afterwards, the fitted sub-sampled phase is up-sampled to reduce the ringing effect, and to obtain the full-resolution phase map of non-cross and cross-aberration terms [Figs. 6(h) and 6(i)]. The overall

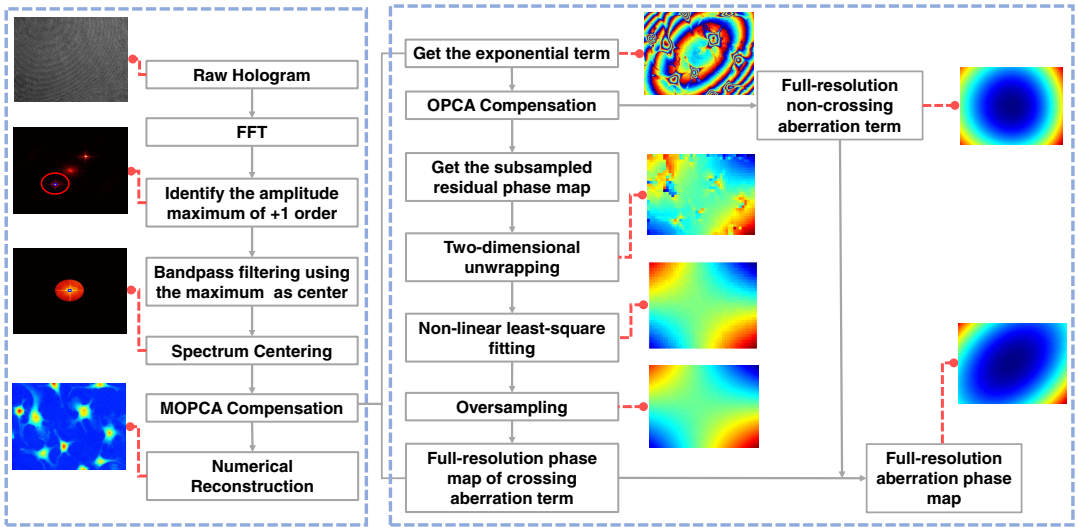

Fig. 5. Block diagram of the compensation process in MOPCA.

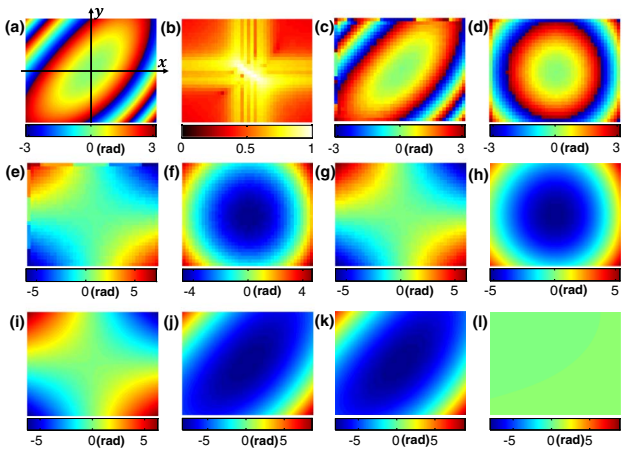

Fig. 6. Results of the MOPCA method for mixed aberration. (a) Wrapped phase of the simulated aberration. (b) Cropped normalized aberration spectrum. (c) Sub-sampled aberration phase map. (d) Sub-sampled phase of the first principal component. (e) Sub-sampled unwrapped phase of the residual aberration apart from that of the first principal component. (f) Fitted phase of the first principal component. (g) Fitted phase of the residual aberration shown in (e). (h) and (i) show the full-resolution phase of the first principal component and that of the residual aberration recovered through up-sampling. (j) shows the full-resolution phase recovered through MOPCA. (k) and (l) show the unwrapped phase of the original aberration and the difference between phases shown in (j) and (k).

Table 1. Time Cost and RMSE of the Aberration Compensation for $Q(x, y)$ Using Zernike Polynomial Fitting, Least-Square Fitting, and MOPCA

Method	Time (s)	RMSE (rad)
Zernike polynomial fitting	2.36	0.027
Least-square fitting	78.42	0.712
MOPCA	0.10	0.007

aberration phase map [Fig. 6(j)] can be obtained by adding the two phase maps together. Compared with the phase obtained by unwrapping the original aberration phase [Fig. 6(k)], it can be found that the phase difference [Fig. 6(l)] of the recovered full-resolution phase can be neglected.

The time required for phase aberration compensation after phase unwrapping using Zernike polynomial fitting, least-square fitting, and MOPCA is shown in Table 1, using MATLAB R2014a for simulation on a 2.30 GHz laptop. Compared to the other two traditional methods, the proposed MOPCA method has a considerable speed improvement, and the RMSE of the phase recovered using the MOPCA method is 0.007(rad), which can be ignored compared with the original phase and meets the accuracy requirement.

4. EXPERIMENT

Based on previous discussions, two experiments were performed where MOPCA was implemented to remove the phase aberration. In the first experiment, the hologram was taken with a blank sample placed on the stage of a holographic microscope. In the other experiment, the hologram was taken with HeLa cell samples on the stage. In order to illustrate the advantages of the proposed method, the double-exposure approach, least-square fitting method, and Zernike polynomial fitting method are also implemented to remove the phase aberration. In the experiments, we used a camera (DMK 23U274, 1600x1200) with a pixel size of 4.4 μm, and the images were obtained with the objective lens (Olympus UPLFLN, 0.3 NA) at a magnification of 10 and a laser (Thorlabs HNLS008R-EC) with a wavelength of 633 nm.

In the first experiment, MOPCA (in which the size of the cropped spectrum is 40 × 30), double exposure, least-square fitting using the full-resolution image, and Zernike polynomial fitting using the first nine Zernike polynomial terms were implemented to remove aberrations in a hologram obtained with a blank sample on the stage. The results of each step are shown to illustrate the experimental procedure. The hologram captured by the camera is shown in Fig. 7(a), the spectrum of which is shown in Fig. 7(b). The full-resolution phase map [Fig. 7(e)] is obtained after spectrum centering [Fig. 7(c)] and IFT. Here, we need to point out that in order to achieve higher accuracy and more details in phase reconstruction, the entire +1 spectrum is intercepted [Fig. 7(c)]. The area in the center of the +1 spectrum with a size of 40 × 30 [Fig. 7(d)] is cropped to perform IFT. After IFT, the sub-sampled phase is recovered [Fig. 7(f)], and PCA is performed afterwards. The phase of the first principal component is shown in Fig. 7(g). Afterwards, the phase of the first principal component and the residual component is fitted and up-sampled [Figs. 7(i) and 7(j)] to avoid ringing effect. The overall aberration phase map [Fig. 7(k)] is obtained by adding the two aberration terms together. Finally, the phase of the aberration term is compensated and the reconstructed phase without aberration [Fig. 7(o)] is obtained. Compared with the original aberration phase map, the compensated phase map without aberration has a much smoother background [Fig. 7(o)], and the phase compensation results of the double-exposure approach, Zernike polynomial fitting, and least-square fitting are shown in Figs. 7(l)–7(n), respectively.

To show the details of the phase-compensation results, the aberration-free phase map obtained using double exposure is used as the standard value. The residual phase, which is the difference between the phase recovered using Zernike polynomial fitting, least-square fitting, and MOPCA and that recovered using double-exposure approach resulting from the parasitic interference and laser speckle noise (which are considered as phase aberration in the double-exposure approach indiscriminately) are shown in Figs. 7(p)–7(r), respectively.

The time spent on aberration compensation using Zernike polynomial fitting, least-square fitting, and MOPCA as proposed in this paper after phase unwrapping, as well as the RMSEs between the phase recovered using these three methods and the double-exposure approach, are shown in Table 2. It can be seen that the phase recovered using these methods are accurate, and the MOPCA method has an obvious advantage in operation speed.

Next, MOPCA (in which the spectrum size is 48 × 36 to meet the energy requirement), double exposure, Zernike polynomial

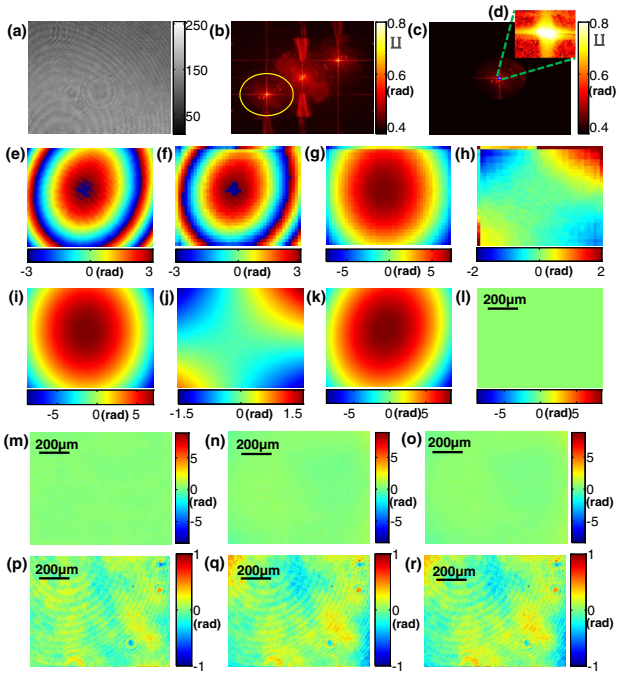

Fig. 7. Phase-aberration compensation using MOPCA and three other traditional methods with a blank sample on the stage. (a) Hologram shot by the camera. (b) Normalized spectrum of the hologram. (c) Centered +1 order spectrum. (d) Full-resolution phase map with aberration. (e) Cropped sub-sampled +1 order spectrum. (f) Sub-sampled phase map. (g) Phase of the first principal component. (h) Residual phase map. (i) Full-resolution phase map recovered through up-sampling. (j) Full-resolution phase of the residual aberration. (k) Full-resolution aberration phase map. (l) shows the aberration-free phase map using double exposure method, which is at the same scale with (k). (m), (n), and (o) show the phase-compensation results of Zernike polynomial fitting, least-square fitting, and MOPCA, respectively. (p), (q), and (r) show the corresponding residual phases between the aberration-free phases shown in (m), (n), and (o) and that shown in (l).

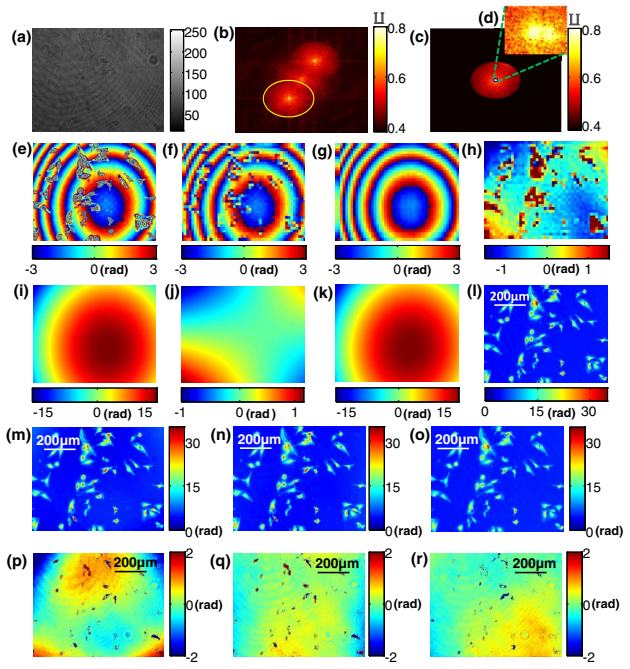

Fig. 8. Phase-aberration compensation on HeLa cells using the proposed MOPCA algorithm and three other traditional methods. (a) Hologram shot by camera. (b) Normalized spectrum of the hologram. (c) Centered +1 order spectrum. (d) Cropped sub-sampled +1 order spectrum. (e) Full-resolution phase map with aberration. (f) Sub-sampled phase map. (g) Phase of the extracted first principal component. (h) Residual phase map. (i) Full-resolution phase map recovered through up-sampling. (j) Full-resolution phase of the residual aberration. (k) Full-resolution phase map of the aberration. (l) Aberration-free phase map of HeLa cells using double-exposure method. (m), (n), and (o) show the phase-compensation results of Zernike polynomial fitting, least-square fitting, and MOPCA, respectively. (p), (q), and (r) show the corresponding residual phase between the phase shown in (m), (n), and (o) and that shown in (l).

fitting (using the first nine Zernike polynomial terms), and least-square fitting using the full-resolution image were performed on the hologram of HeLa cells. Similarly, we show the results of each step in MOPCA. Figure 8(a) shows the image shot by the camera, the spectrum of which is shown in Fig. 8(b). The full-resolution phase map [Fig. 8(e)] can be obtained after spectrum centering [Fig. 8(c)] and IFT. Here, in order to achieve more details in phase reconstruction, the entire +1 spectrum is intercepted. We cropped the area at the center of the +1 spectrum with a size of 40 × 30 [Fig. 8(d)] to perform IFT. After IFT, the sub-sampled phase map was recovered [Fig. 8(f)]. Then, PCA was performed on the sub-sampled image and the phase of the first principal component is shown in Fig. 8(g). Afterwards, the phase of the first principal component and the residual phase are fitted, and in order to avoid ringing effect, the phase is up-sampled to get the full-resolution phase map [Figs. 8(i) and 8(j)]. The overall aberration phase map [Fig. 8(k)] is obtained by adding the two aberration maps together. Finally, the phase of aberration term is compensated and the aberration-free phase map of the HeLa cells [Fig. 8(o)] is obtained. The aberration-free phase map of HeLa cells recovered through the double-exposure approach, Zernike polynomial fitting, and least-square fitting are shown in Figs. 8(l)–8(n), respectively. To further show the details of the phase-compensation results, the aberration-free phase map obtained using double exposure is used as the standard value, and the residual phase between the phase recovered using Zernike polynomial fitting, least-square fitting, and MOPCA is shown in Figs. 8(p)–8(r). It should be noted that some object information also appears in all phase residual maps; this is due

Table 2. Time Spent on the Phase-Aberration Compensation and RMSE between the Phase Recovered Using Zernike Polynomial Fitting, Least-Square Fitting, and MOPCA and that Recovered Through Double-Exposure Approach with a Blank Sample Placed on the Stage

Method	Time (s)	RMSE (rad)
Zernike polynomial fitting	1.57	0.131
Least-square fitting	15.87	0.162
MOPCA	0.14	0.167

Table 3. Time Spent on the Phase-Aberration Compensation and RMSE between the Phase Recovered Using Zernike Polynomial Fitting, Least-Square Fitting, and MOPCA and that Recovered through Double-Exposure Approach with HeLa Cell Samples Placed on the Stage

Method	Time (s)	RMSE (rad)
Zernike polynomial fitting	1.62	1.071
Least-square fitting	16.57	0.939
MOPCA	0.14	0.782

to the phase-unwrapping errors around cell regions with significant phase wraps.

It can also be found in experiment that if PCA is performed on the full-resolution image, the object's information will lead to a worse result when fitting the residual cross terms, indicating that the object's phase affects the fitting accuracy to some extent. It is illustrated that intercepting a small +1 spectrum and fitting the sub-sampled aberrations can effectively avoid the influence of the phase information induced by the object on the aberration fitting when the tested object has a high spatial frequency. However, if the object has a phase of low frequency which is close to that of the aberration, it is difficult to effectively remove the influence of the object's phase on the aberration fitting by intercepting the low-frequency domain.

The time spent on the aberration compensation using Zernike polynomial fitting, least-square fitting, and MOPCA as proposed in this paper after phase unwrapping, as well as the RMSEs between the phase recovered using the latter three methods and that recovered through the double-exposure approach, are shown in Table 3. From the phase-compensation results of these three methods, it can be seen that using the proposed MOPCA method not only has higher accuracy compared to the other traditional methods, but also has a considerable speed improvement.

5. CONCLUSION

In summary, this paper proves that the OPCA aberration compensation method is suitable for the compensation of high-order non-cross-aberration terms in DHM, and since the PCA results of aberration term xy are not concentrated in one single component, it is not possible to use PCA-based compensation methods alone to compensate for cross-aberration terms. Therefore, for cases in which non-cross-aberration and cross-aberration terms coexist, this paper proposes a multi-step numerical aberration-compensation method based on OPCA and sub-sampling. For cross-aberration terms existing in the hologram, since the sub-sampling method reduces the size of the image for 2D fitting, the speed is greatly accelerated. Moreover, because of the complexity of 2D phase unwrapping, using a smaller image for phase unwrapping not only accelerates the speed, but also improves the accuracy.

Although only cross-aberration term xy is discussed in this paper and other high-order cross-aberration terms are disregarded, this method should nevertheless be extendable to the compensation of other such terms, such as x^2y. That is, when compensating aberration which contains high-order cross-aberration terms, the fitting can be achieved by changing the fitting order of the residual aberration-fitting process in the MOPCA method. In addition, as the order of aberration increases, the spectrum shape changes correspondingly. Therefore, when sub-sampling high-order aberration terms, it is necessary to pay attention to whether the high-frequency components contained in the intercepted spectrum are sufficient. Certainly, we could add a step of adaptively selecting the +1 order aberration spectrum to satisfy the condition that the energy of the selected aberration spectrum must account for more than 80% of the total energy of the full-resolution spectrum. This would not only improve the aberration-compensation accuracy, but also make MOPCA a completely adaptive compensation method for all aberration types without any manual intervention. This may be our next research direction.

When samples with low phase variation are tested, the method we propose may not provide appropriate compensation, in contrast to the compensation method based on deep-learning mentioned in Ref [30]. Additionally, our method is not efficient for punctual defects; these are problems we are going to solve in the future.

Funding. National Natural Science Foundation of China (NSFC) (11574152, 61505081, 61722506); Final Assembly "13th Five-Year Plan" Advanced Research Project of China (30102070102); Equipment Advanced Research Fund of China (61404150202); National Defense Science and Technology Foundation of China (0106173); Key Research and Development Program of Jiangsu Province, China (BE2017162); "Six Talent Peaks" Project of Jiangsu Province, China (2015-DZXX-009); "333 Engineering" Research Project of Jiangsu Province, China (BRA2016407); Fundamental Research Funds for the Central Universities (30916011322, 30917011204); Outstanding Youth Foundation of Jiangsu Province of China (BK20170034).

[†]These authors contributed equally to this work.

REFERENCES

1. B. Rappaz, P. Marquet, E. Cuche, Y. Emery, C. Depeursinge, and P. J. Magistretti, "Measurement of the integral refractive index and dynamic cell morphometry of living cells with digital holographic microscopy," Opt. Express **13**, 9361–9373 (2005).
2. F. Charrière, A. Marian, F. Montfort, J. Kuehn, T. Colomb, E. Cuche, P. Marquet, and C. Depeursinge, "Cell refractive index tomography by digital holographic microscopy," Opt. Lett. **31**, 178–180 (2006).
3. B. Rappaz, F. Charrière, C. Depeursinge, P. J. Magistretti, and P. Marquet, "Simultaneous cell morphometry and refractive index measurement with dual-wavelength digital holographic microscopy and dye-enhanced dispersion of perfusion medium," Opt. Lett. **33**, 744–746 (2008).
4. B. Rappaz, A. Barbul, Y. Emery, R. Korenstein, C. Depeursinge, P. J. Magistretti, and P. Marquet, "Comparative study of human erythrocytes by digital holographic microscopy, confocal microscopy, and impedance volume analyzer," Cytometry Part A **73**, 895–903 (2008).
5. P. Langehanenberg, L. Ivanova, I. Bernhardt, S. Ketelhut, A. Vollmer, D. Dirksen, G. K. Georgiev, G. von Bally, and B. Kemper, "Automated three-dimensional tracking of living cells by digital holographic microscopy," J. Biomed. Opt. **14**, 014018 (2009).

6. A. Khmaladze, R. L. Matz, T. Epstein, J. Jasensky, M. M. B. Holl, and Z. Chen, "Cell volume changes during apoptosis monitored in real time using digital holographic microscopy," J. Struct. Biol. **178**, 270–278 (2012).
7. N. Pavillon, J. Kühn, C. Moratal, P. Jourdain, C. Depeursinge, P. J. Magistretti, and P. Marquet, "Early cell death detection with digital holographic microscopy," PloS ONE **7**, e30912 (2012).
8. B. Kemper, D. D. Carl, J. Schnekenburger, I. Bredebusch, M. Schäfer, W. Domschke, and G. von Bally, "Investigation of living pancreas tumor cells by digital holographic microscopy," J. Biomed. Opt. **11**, 034005 (2006).
9. B. Kemper and G. von Bally, "Digital holographic microscopy for live cell applications and technical inspection," Appl. Opt. **47**, A52–A61 (2008).
10. Y. Wang, Y. Yang, D. Wang, L. Ouyang, Y. Zhang, J. Zhao, and X. Wang, "Morphological measurement of living cells in methanol with digital holographic microscopy," Comput. Math. Methods Med. **2013**, 715843 (2013).
11. P. Marquet, C. Depeursinge, and P. J. Magistretti, "Exploring neural cell dynamics with digital holographic microscopy," Annu. Rev. Biomed. Eng. **15**, 407–431 (2013).
12. T. A. Mir and H. Shinohara, "Label-free observation of three-dimensional morphology change of a single pc12 cell by digital holographic microscopy," Anal. Biochem. **429**, 53–57 (2012).
13. D. Carl, B. Kemper, G. Wernicke, and G. von Bally, "Parameter-optimized digital holographic microscope for high-resolution living-cell analysis," Appl. Opt. **43**, 6536–6544 (2004).
14. N. Pavillon, J. Kühn, P. Jourdain, C. D. Depeursinge, P. J. Magistretti, and P. Marquet, "Cell death and ionic regulation detection with digital holographic microscopy," in *Digital Holography and Three-Dimensional Imaging* (Optical Society of America, 2011), paper DTuC25.
15. Y. Fang, C. Y. Iu, C. N. Lui, Y. Zou, C. K. Fung, H. W. Li, N. Xi, K. K. Yung, and K. W. Lai, "Investigating dynamic structural and mechanical changes of neuroblastoma cells associated with glutamate-mediated neurodegeneration," Sci. Rep. **4**, 7074 (2014).
16. N. Warnasooriya, F. Joud, P. Bun, G. Tessier, M. Coppey-Moisan, P. Desbiolles, M. Atlan, M. Abboud, and M. Gross, "Imaging gold nanoparticles in living cell environments using heterodyne digital holographic microscopy," Opt. Express **18**, 3264–3273 (2010).
17. H. Sun, B. Song, H. Dong, B. Reid, M. A. Player, J. Watson, and M. Zhao, "Visualization of fast-moving cells in vivo using digital holographic video microscopy," J. Biomed. Opt. **13**, 014007 (2008).
18. X. Wang, W. Sun, Y. Cui, J. Ye, S. Feng, and Y. Zhang, "Complete presentation of the Gouy phase shift with the THz digital holography," Opt. Express **21**, 2337–2346 (2013).
19. X. Gao, C. Li, and G. Fang, "Study of image reconstruction for terahertz indirect holography with quasi-optics receiver," J. Opt. Soc. Am. A **30**, 1291–1296 (2013).
20. M. K. Kim, "Digital holographic microscopy," in *Digital Holographic Microscopy* (Springer, 2011), pp. 149–190.
21. C. Zuo, Q. Chen, W. Qu, and A. Asundi, "Phase aberration compensation in digital holographic microscopy based on principal component analysis," Opt. Lett. **38**, 1724–1726 (2013).
22. W. Zhou, Y. Yu, and A. Asundi, "Study on aberration suppressing methods in digital micro-holography," Opt. Lasers Eng. **47**, 264–270 (2009).
23. J. Di, J. Zhao, W. Sun, H. Jiang, and X. Yan, "Phase aberration compensation of digital holographic microscopy based on least squares surface fitting," Opt. Commun. **282**, 3873–3877 (2009).
24. C. J. Mann, L. Yu, C.-M. Lo, and M. K. Kim, "High-resolution quantitative phase-contrast microscopy by digital holography," Opt. Express **13**, 8693–8698 (2005).
25. A. Anand, V. K. Chhaniwal, and B. Javidi, "Real-time digital holographic microscopy for phase contrast 3D imaging of dynamic phenomena," J. Display Technol. **6**, 500–505 (2010).
26. W. Qu, C. O. Choo, V. R. Singh, Y. Yingjie, and A. Asundi, "Quasi-physical phase compensation in digital holographic microscopy," J. Opt. Soc. Am. A **26**, 2005–2011 (2009).
27. E. Sánchez-Ortiga, P. Ferraro, M. Martnez-Corral, G. Saavedra, and A. Doblas, "Digital holographic microscopy with pure-optical spherical phase compensation," J. Opt. Soc. Am. A **28**, 1410–1417 (2011).
28. Y. Liu, Z. Wang, J. Li, J. Gao, and J. Huang, "Total aberrations compensation for misalignment of telecentric arrangement in digital holographic microscopy," Opt. Eng. **53**, 112307 (2014).
29. L. Miccio, D. Alfieri, S. Grilli, P. Ferraro, A. Finizio, L. De Petrocellis, and S. Nicola, "Direct full compensation of the aberrations in quantitative phase microscopy of thin objects by a single digital hologram," Appl. Phys. Lett. **90**, 041104 (2007).
30. T. Nguyen, V. Bui, V. Lam, C. B. Raub, L.-C. Chang, and G. Nehmetallah, "Automatic phase aberration compensation for digital holographic microscopy based on deep learning background detection," Opt. Express **25**, 15043–15057 (2017).
31. T. Colomb, J. Kühn, F. Charriere, C. Depeursinge, P. Marquet, and N. Aspert, "Total aberrations compensation in digital holographic microscopy with a reference conjugated hologram," Opt. Express **14**, 4300–4306 (2006).
32. P. Ferraro, S. De Nicola, A. Finizio, G. Coppola, S. Grilli, C. Magro, and G. Pierattini, "Compensation of the inherent wave front curvature in digital holographic coherent microscopy for quantitative phase-contrast imaging," Appl. Opt. **42**, 1938–1946 (2003).
33. T. Colomb, F. Montfort, J. Kühn, N. Aspert, E. Cuche, A. Marian, F. Charrière, S. Bourquin, P. Marquet, and C. Depeursinge, "Numerical parametric lens for shifting, magnification, and complete aberration compensation in digital holographic microscopy," J. Opt. Soc. Am. A **23**, 3177–3190 (2006).
34. T. Colomb, E. Cuche, F. Charrière, J. Kühn, N. Aspert, F. Montfort, P. Marquet, and C. Depeursinge, "Automatic procedure for aberration compensation in digital holographic microscopy and applications to specimen shape compensation," Appl. Opt. **45**, 851–863 (2006).
35. G. Zhang, T. Guan, Z. Shen, X. Wang, T. Hu, D. Wang, Y. He, and N. Xie, "Fast phase retrieval in off-axis digital holographic microscopy through deep learning," Opt. Express **26**, 19388–19405 (2018).
36. J. Sun, Q. Chen, Y. Zhang, and C. Zuo, "Optimal principal component analysis-based numerical phase aberration compensation method for digital holography," Opt. Lett. **41**, 1293–1296 (2016).

219.230.65.77 (on 2022-04-07 05:21:36)